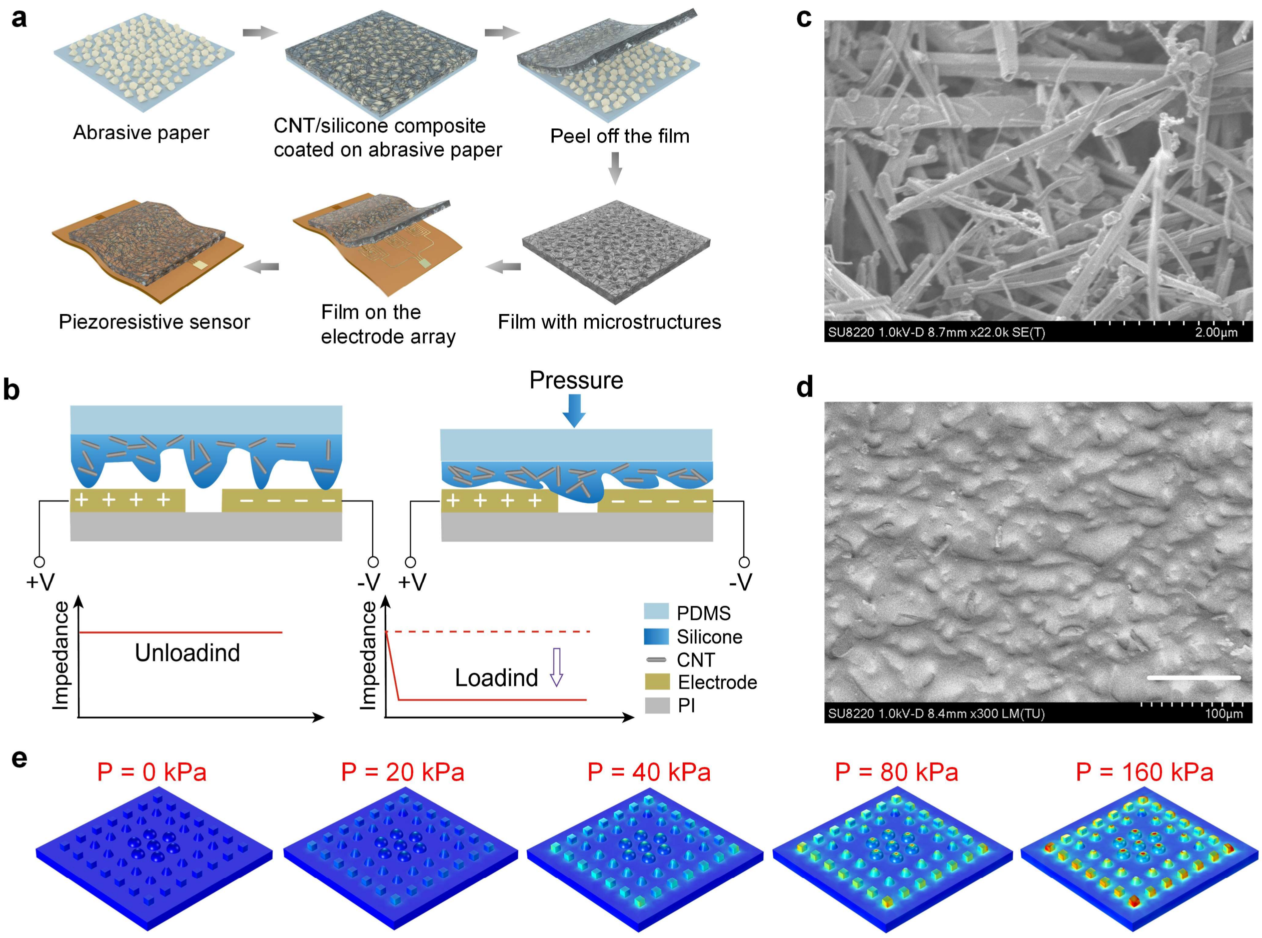

Extended Data Fig. 1 | Fabrication and characterization of flexible piezoresistive films. a, Schematic illustration of the fabrication process. The mixture of silicone elastomer and carbon nanotubes (CNTs) was evenly scraped onto an abrasive paper using a knife coater to form the piezoresistive film with spinous microstructures. The CNT/silicone composite-based piezoresistive film and an interdigitated surface electrode array are then integrated as the piezoresistive tactile sensor matrix. **b**, Schematic illustration of the operation of the flexible piezoresistive sensor before and after applying the pressure. Applying forward pressure to the piezoelectric film causes a small change in its thickness, resulting in slight physical migration between nanotubes. This changes the resistance of the original conductive path and produces a curve showing the relation between pressure and resistance. **c**, Scanning electron microscopy (SEM) micrographs of the carbon nanotubes (CNT). **d**, SEM image of the prepared piezoresistive film, showing details of the microstructure. **e**, Stress distribution of the finite element model of the microstructured film under different applied pressure from 0-160 kPa.

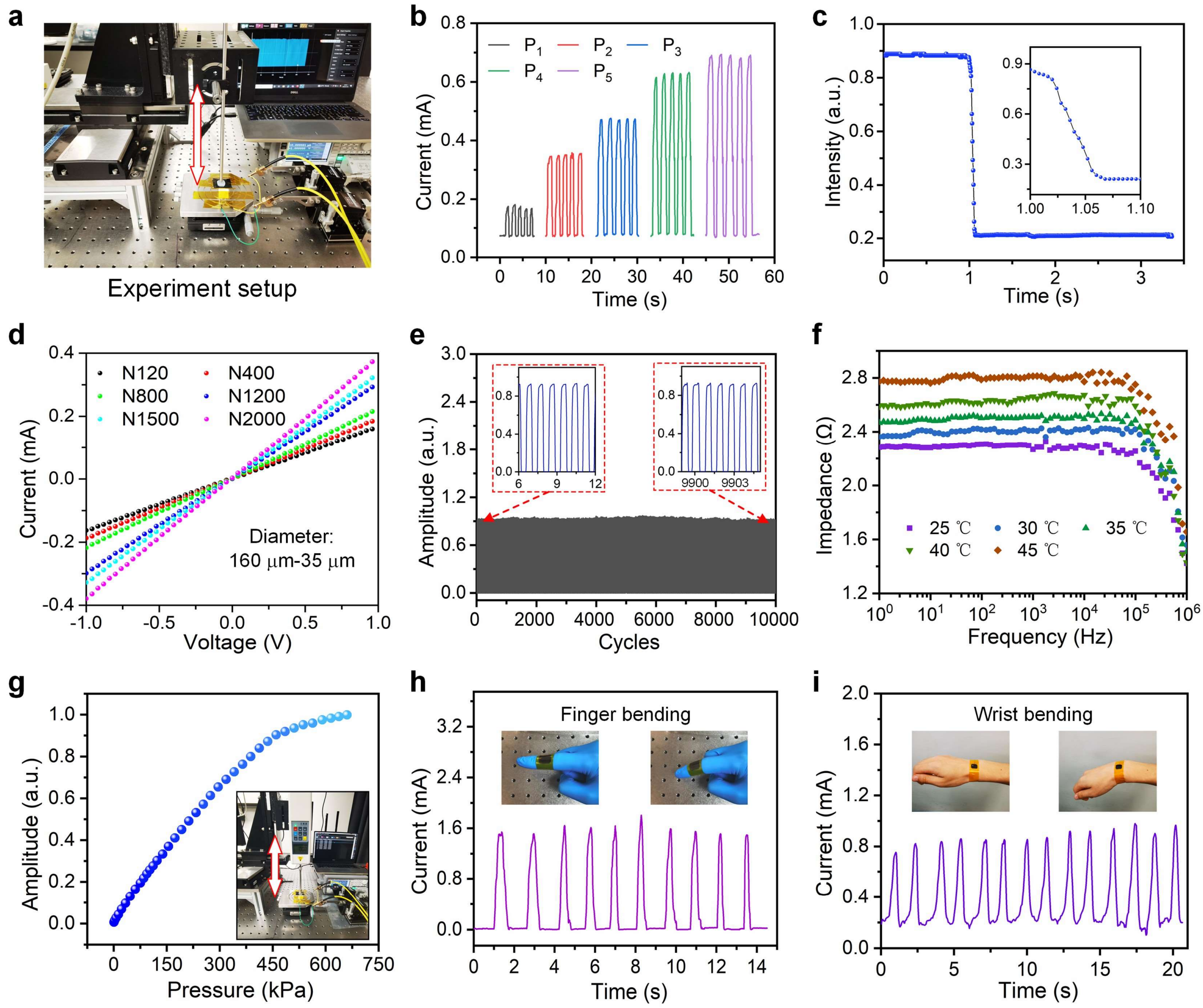

Extended Data Fig. 2 | Characterization of the flexible piezoresistive sensor. **a**, A snapshot of the characterization platform, including a three-axis motorized stage for repetitive loading and unloading of pressure, a source meter for current measurements, and a computer for real-time data recording. **b**, Current versus time curves of the CNT/silicone composite-based tactile sensor processed using abrasive paper No.1200 under different pressures. **c**, Temporal response of the sensor to a sudden pressure. The inset shows detailed information about the recovery time. **d**, I–V curves of the sensor (15 wt% CNT concentration), as processed using abrasive paper with different grit sizes (No.120, 400, 800, 1200, 1500, and 2000). **e**, Stability of the sensor measured by subjecting it to 10,000 compression and release cycles, highlighting its ability to maintain consistent performance over extended usage. **f**, Bode plots of the piezoresistive film (15 wt % CNT concentration) at various temperatures. **g**, Sensitivity of the piezoresistive sensor processed using abrasive paper No.1200, plotted as the normalized current signal as a function of pressure. The inset shows the test setup with a force gauge used to quantify the applied pressure. **h** and **i**, Applications of the piezoresistive film in real-time monitoring of human activity and detection of small physical signals. The signal responses in the form of changes in current are generated by finger bending (h) and wrist bending (i).

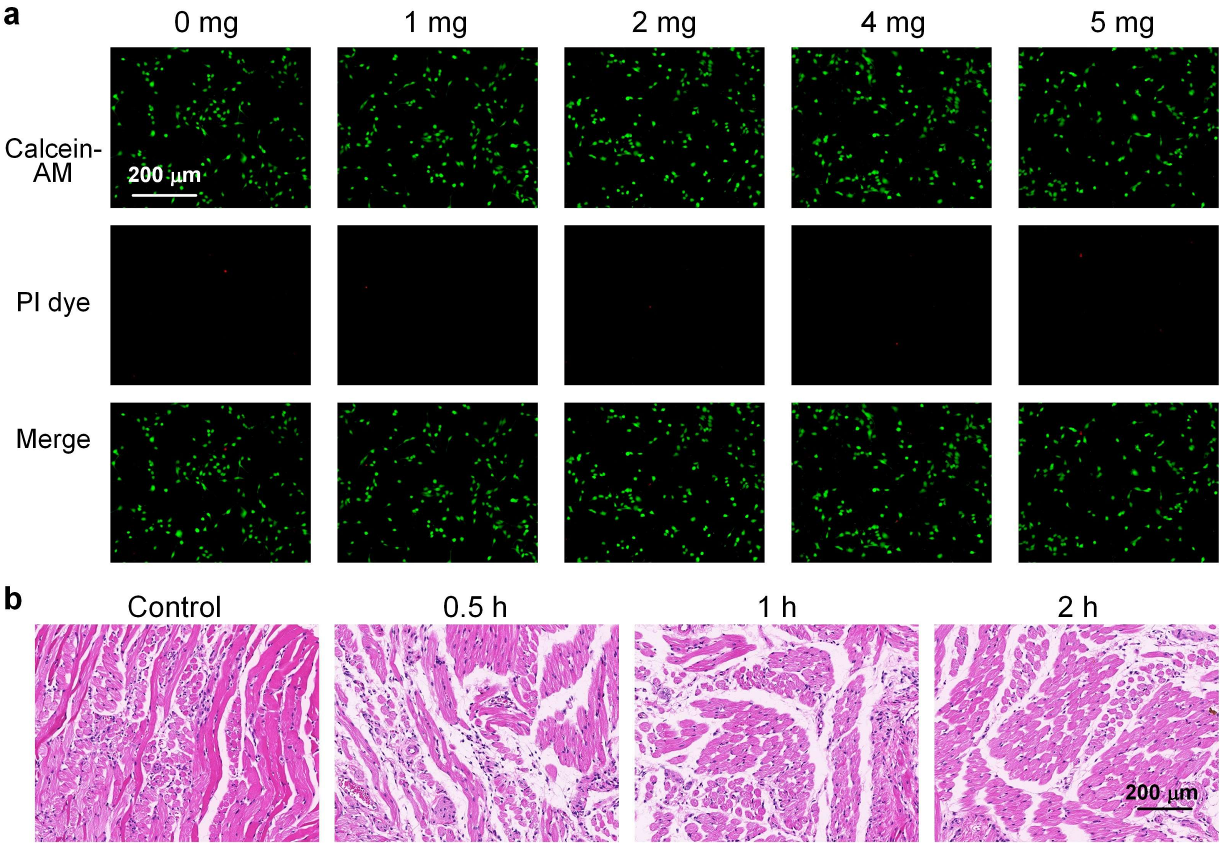

Extended Data Fig. 3 | Biocompatibility characterization of the flexible piezoresistive sensor. **a**, Cytotoxicity analysis via fluorescence imaging of Calcein-AM/PI-labeled live cells (green) and dead cells (red) with varying amounts (0-5 mg) of sensor materals. **b**, Mechanical damage analysis. The tongues of the mice were held with forceps, and the sensor was placed on the tongues for durations of 0.5, 1, and 2 h. The experimental results showed no signs of hemorrhage, inflammation and nuclear pyknosis in the tongue surface cells, confirming the good biocompatibility of sensor materials.

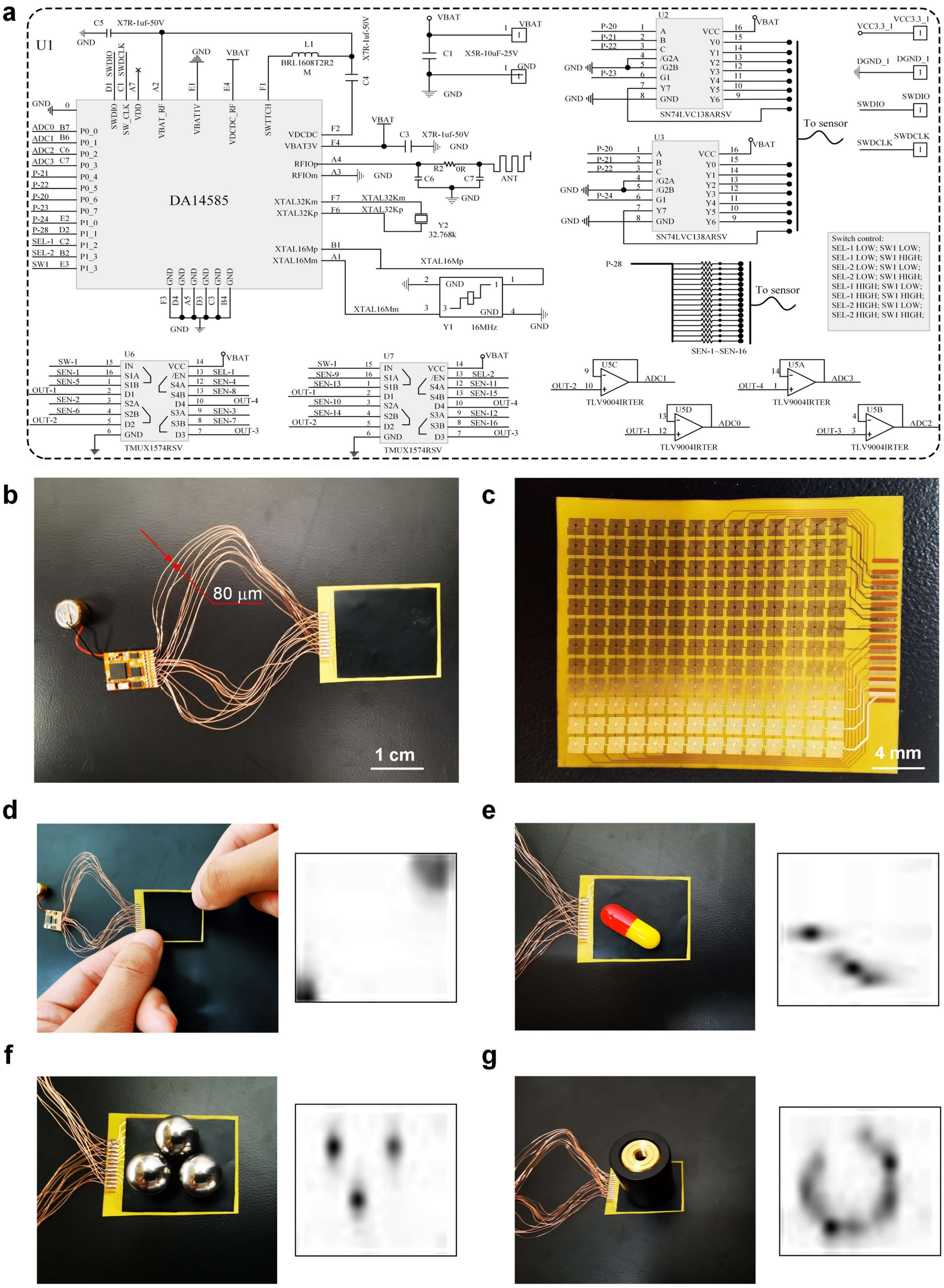

Extended Data Fig. 4 | Circuit architecture and stress testing of the tactile oPad using different objects. a, Circuit schematic for data acquisition and communication. The active row during readout is selected by grounding one of the 16 single-pole double throw (SPDT) switches. A 3-to-8-line decoder is used to select one of the 16 columns at a time. **b**, Tactile sensor array integrated with the flexible circuit using copper-insulated flexible wires (80 µm diameter) and a small lithium battery as the power supply. **c**, Completed CNT/silicone composite-based tactile sensor array before machining into the shape of a mouthguard. **d-f**, Sample recordings of four objects on a regular 12 × 14 array on a flat surface. Resting patterns of these objects are clearly visible.

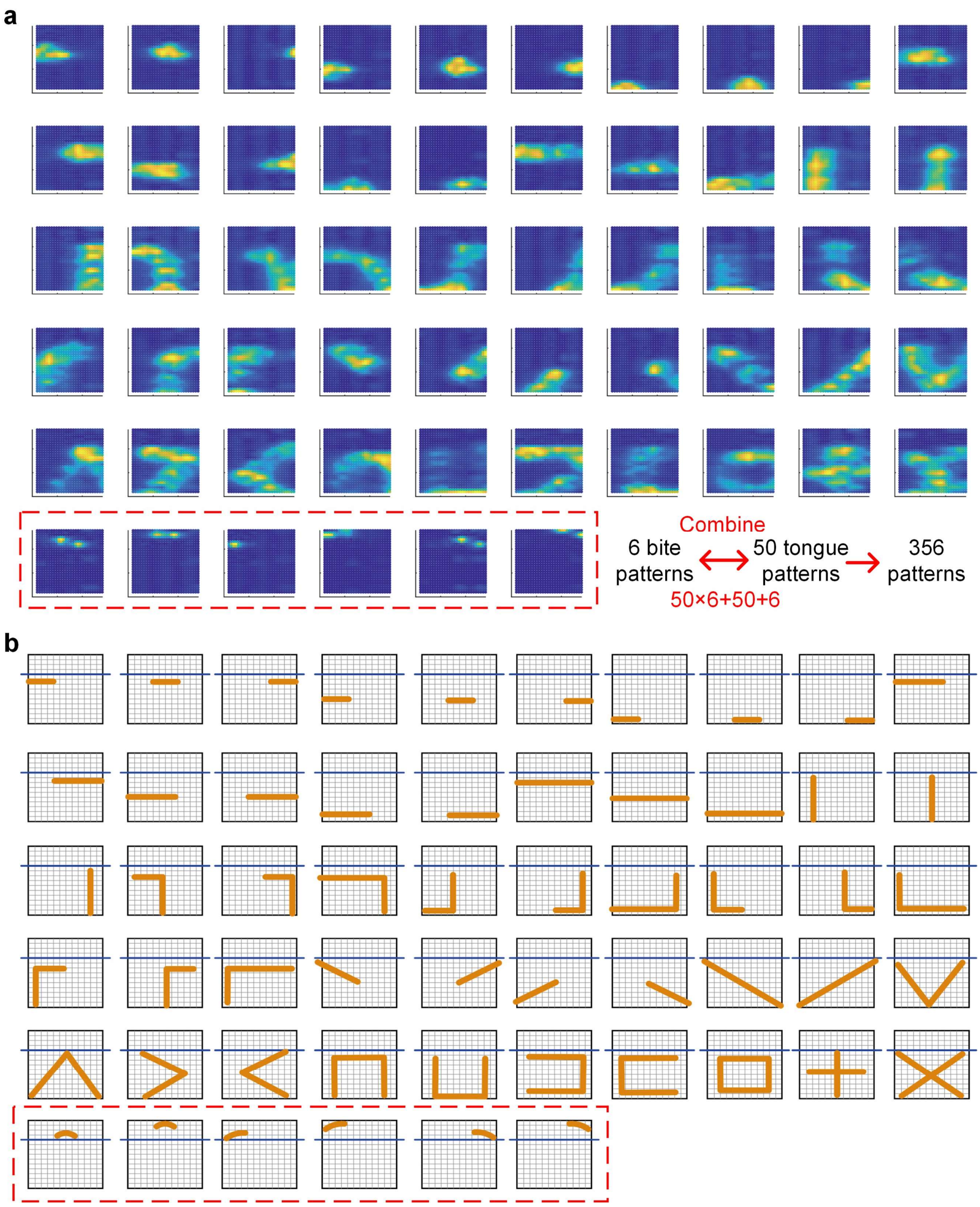

Extended Data Fig. 5 | Design and actual obtained images of 56 patterns generated by tongue sliding and teeth biting. a, Images of 50 tongue sliding patterns and 6 teeth occlusal patterns. Since the tongue sliding and teeth occlusal behaviors are independent, 50 × 6 = 300 different patterns can be generated by synergistic use of the teeth and tongue. Thus, using the tongue alone, the teeth alone, and the combined use of both, a total of 356 patterns are obtained. **b**, Rational design of different patterns according to the correlation between different parts of the sensor array.

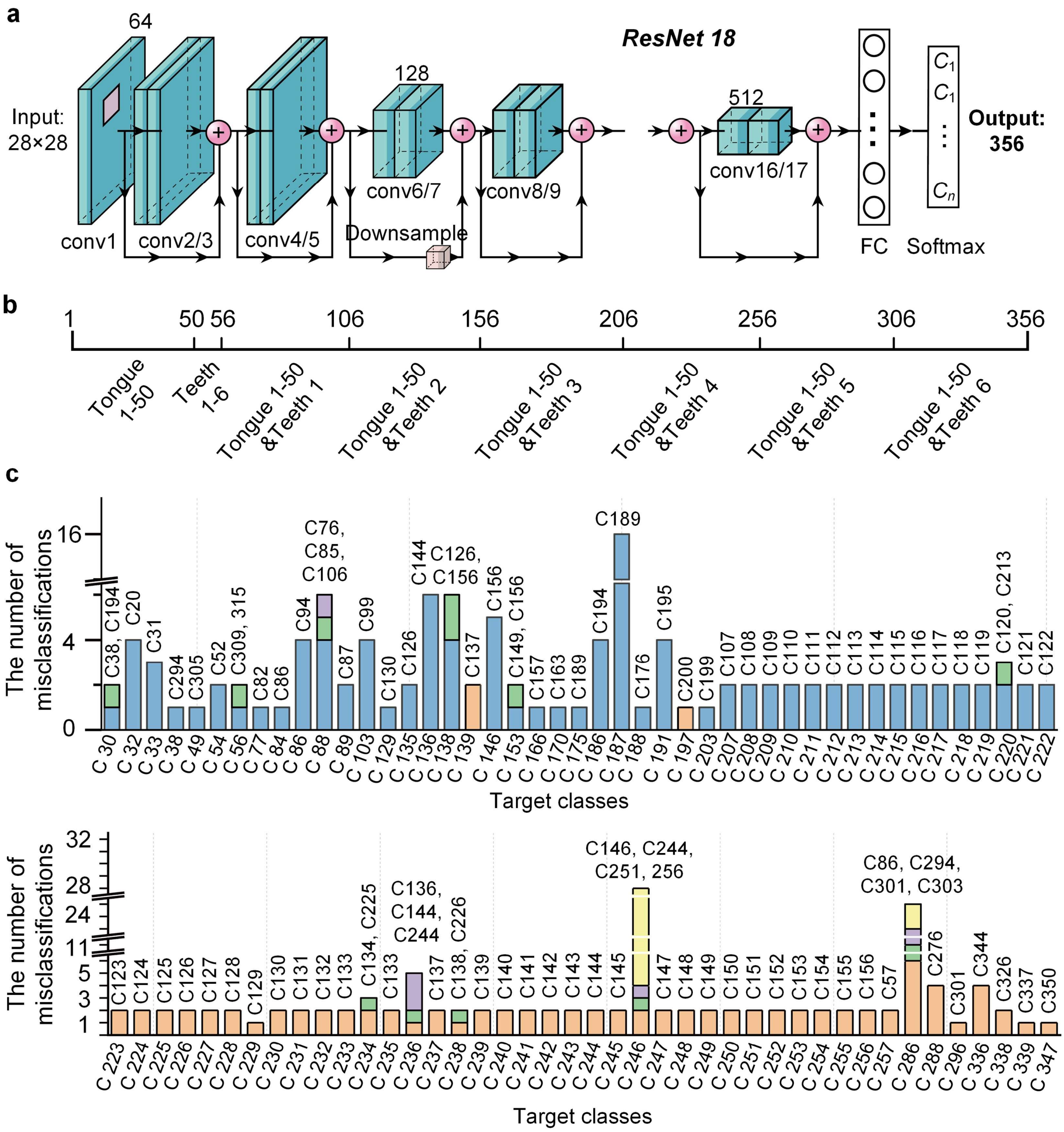

Extended Data Fig. 6 | Results of the CNN network trained on 356 patterns. a, Architecture of the CNN pattern identification network using input *N* arrays of tactile data (28 × 28 array). The data matrix from 14 × 12 sensors are interpolated into 28 × 28 pixel images by algorithm. The network consists of 17 convolutional layers and a fully connected layer, and the last layer uses the softmax function for classification. **b**, Concrete composition of 356 patterns. **c**, Misclassified results using *Resnet18* for 356 patterns, and each pattern has 70 sets of test data. To simplify the presentation, only the misclassified data are listed. The abscissa in the figure represents the target class, the ordinate indicates the number of misclassified data out of total 70 data points, and the superimposed histogram shows the number of misclassifications for each class.

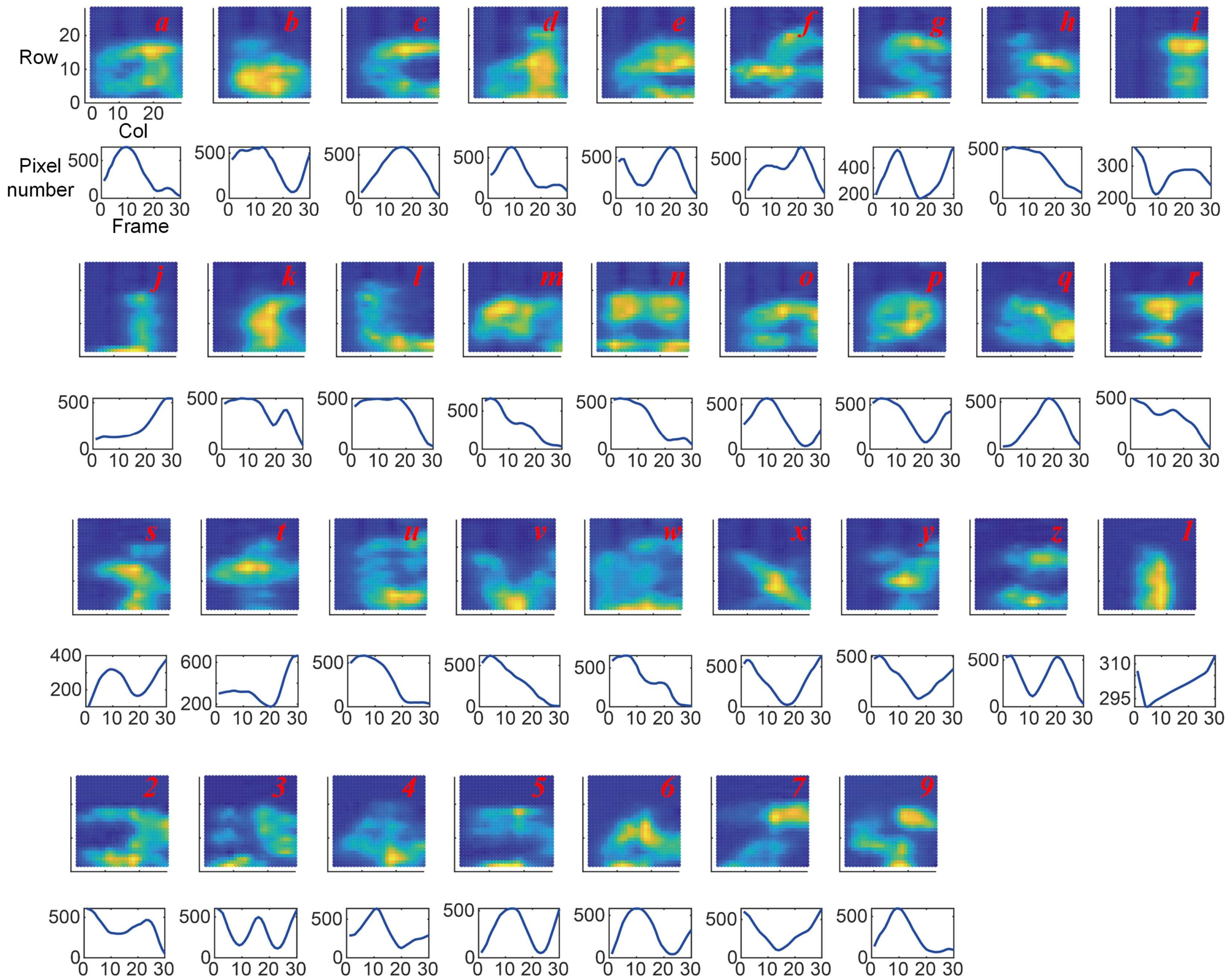

Extended Data Fig. 7 | Real images of 26 English letters and 8 Arabic numerals generated by tongue sliding, along with the corresponding time series curves for each pattern. The number "8" can be replaced by other simple patterns in practical applications due to its complicated strokes.

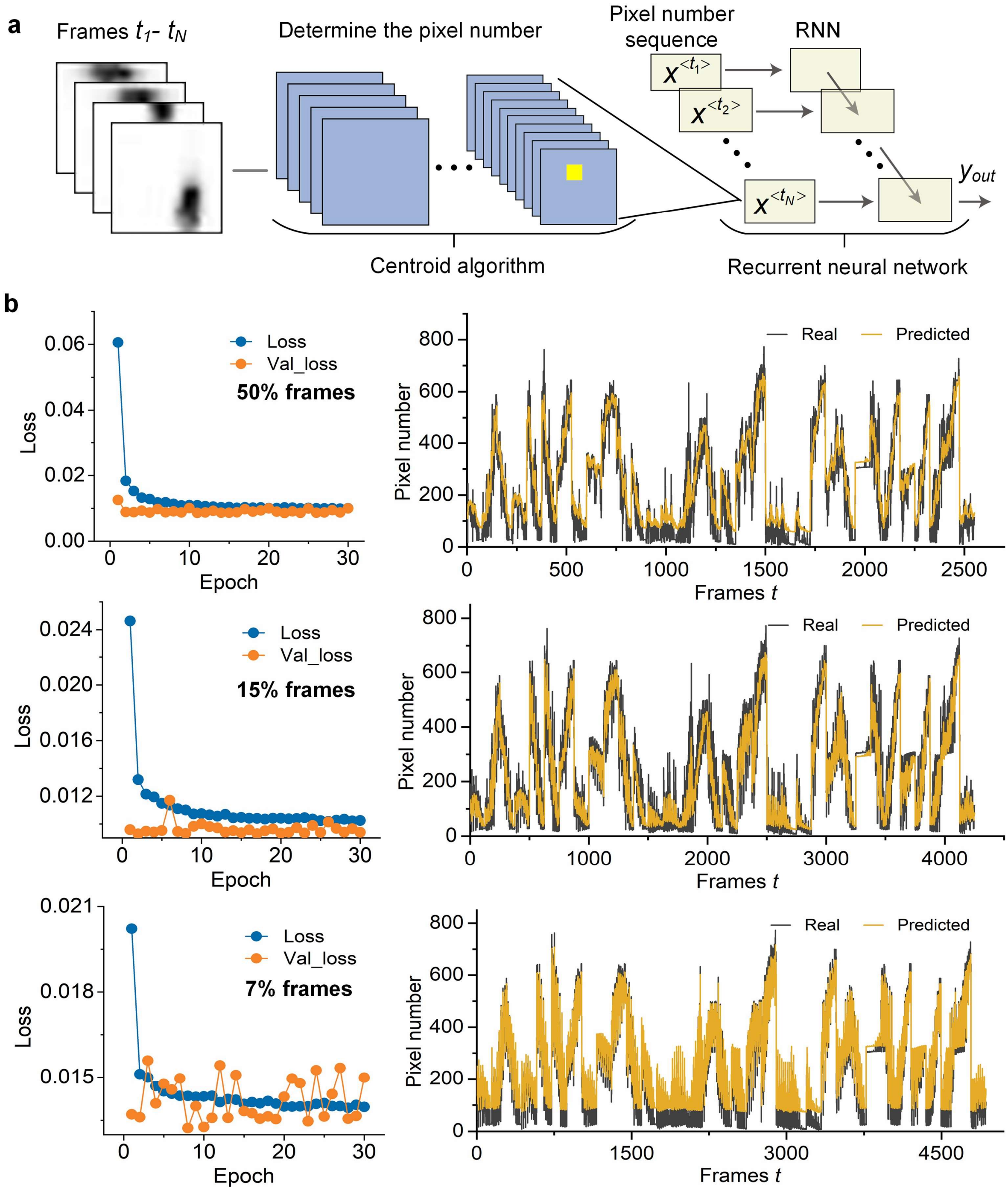

Extended Data Fig. 8 | RNN network structure and prediction results for 34 different characters. **a,** Architecture of the RNN used for character prediction, with N frames of images as input. **b**, Comparison of prediction results using different portions (50%, 15%, and 7%) of the data sequence, including the root mean square error between the predicted data and real data at 30 epochs (left), and the curve depicting the final predicted sequence and the real sequence (right).

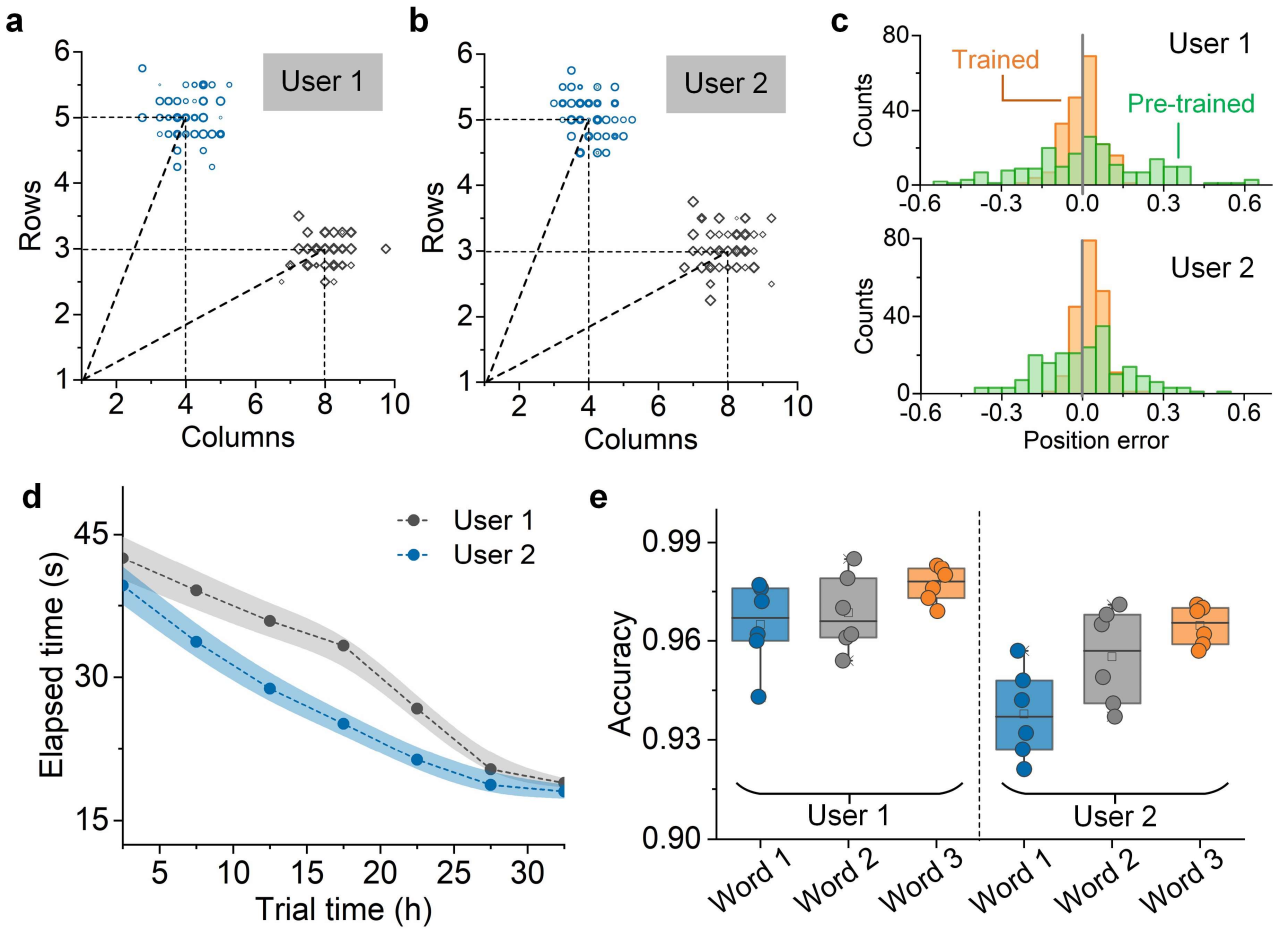

Extended Data Fig. 9 | Assessment of the effectiveness of the machine learning-based tactile oPad on specific tasks performed by two users. a, and **b,** Mouse control efficiency. Tongue pressure point localization results for two users in 100 trials, sliding their tongue from pixel (0, 0) to pixel (4, 5) to pixel (8, 3). The size of the sensor data matrix is interpolated to 28×28, with tongue position localized using the centroid algorithm. **c**, Comparison of localization errors in the column direction before and after training. **d**, Total time taken to complete typing tasks versus training frequency. **e,** Control accuracy for typing tasks.